

Surface-Functionalized Silicon Nanoparticles as Contrast Agents for Photoacoustic Microscopy Imaging

Zhanhong Ye,[†] Prateek K. Srivastava,[‡] Yisu Xu,[†] Wei Wang,[‡] Lili Jing,[‡] Sung-Liang Chen,^{*,†,§} and Chang-Ching Tu^{*,†}

[†]University of Michigan-Shanghai Jiao Tong University Joint Institute, Shanghai Jiao Tong University, Shanghai 200240, China

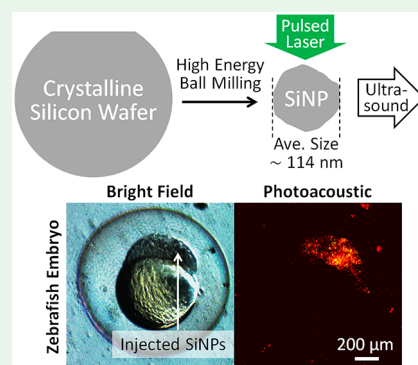
[‡]School of Pharmacy, Shanghai Jiao Tong University, Shanghai 200240, China

[§]State Key Laboratory of Advanced Optical Communication Systems and Networks, Shanghai Jiao Tong University, Shanghai 200240, China

S Supporting Information

ABSTRACT: We demonstrate high contrast optical-resolution photoacoustic microscopy (OR-PAM) imaging by using biocompatible, indirect band gap silicon nanoparticles (SiNPs) as contrast agents. The SiNPs were synthesized by high-energy ball milling of crystalline silicon wafers, followed by hydrosilylation with bifunctional olefinic ligands to enable water solubility and bioconjugation. When uniformly dispersed in water, the SiNPs with an average particle size of about 114 nm showed remarkably high extinction coefficients, more than $2 \times 10^{10} \text{ M}^{-1} \text{ cm}^{-1}$, from the visible to near-infrared spectral range. For the first OR-PAM imaging demonstration, the SiNPs were microinjected to live zebrafish embryonic cells. As the embryo developed, the distribution of the cells carrying the SiNPs can be clearly traced by the spread of the photoacoustic signals. Second, photoacoustic-fluorescence dual-modality imaging was demonstrated on live zebrafish larvae which were microinjected with a mixture of the SiNPs and dextran-rhodamine dyes. Due to the large difference in size, the two agents exhibited very different biodistributions after being injected at the same instant. Third, immuno-photoacoustic imaging, as an autofluorescence-free alternative to the conventional immunofluorescence imaging, was demonstrated on SKOV-3 cancer cells immunostained with the anti-HER2-conjugated SiNPs. Lastly, advantages of the SiNPs compared to other photoacoustic contrast agents were characterized and discussed.

KEYWORDS: silicon nanoparticle, photoacoustic microscopy imaging, zebrafish, cancer cells, high energy ball milling



INTRODUCTION

Photoacoustic imaging, which converts pulsed optical waves into informative ultrasonic emissions, is an emerging biomedical imaging modality due to its noninvasiveness, use of nonionizing radiation, and capability of achieving high contrast while maintaining a good balance between spatial resolution and penetration depth.^{1–3} Photoacoustic microscopy (PAM), as a subset of photoacoustic imaging, employs point-by-point scanning to detect the acoustic waves resulting from the light absorption and the thermoelastic expansion of biological tissues.⁴ A two-dimensional image can be obtained by raster scanning with no need for a complex reconstruction algorithm.

Depending on whether a focused ultrasound transducer for acoustic detection or a focused pulsed laser for photoacoustic excitation is used, PAM can be further categorized into acoustic-resolution PAM (AR-PAM) and optical-resolution PAM (OR-PAM), respectively.^{5,6} AR-PAM overcomes the main limitations in traditional optical microscopy, namely, optical diffraction and tissue scattering, by utilizing diffused photons for excitation, which penetrate tissues beyond the

optical transport mean free path (about 1 mm), and by harnessing ultrasonic waves for imaging, which are far less scattered by tissues than optical light.⁷ The spatial resolution of AR-PAM is typically tens of micrometers. On the other hand, OR-PAM enables higher spatial resolution up to several micrometers at the expense of smaller penetration depth.⁶ In recent years, PAM has been widely applied to various biomedical imaging and sensing applications, such as the observation of oxyhemoglobin saturation and blood flow and diagnosis of breast cancer and melanoma.^{8–10}

The contrast in photoacoustic imaging stems from the fact that individual constituents of biological tissues have different optical absorption characteristics. Based on endogenous light absorbers, such as hemoglobin, fat, and melanin, photoacoustic imaging can reveal not only the anatomical structures but also the physiological functions of tissues.¹¹ For example, tumors with blood perfusion owing to angiogenesis and hypoxia

Received: September 3, 2019

Accepted: November 15, 2019

Published: November 15, 2019

Scheme 1. Synthesis and Functionalization of the SiNPs

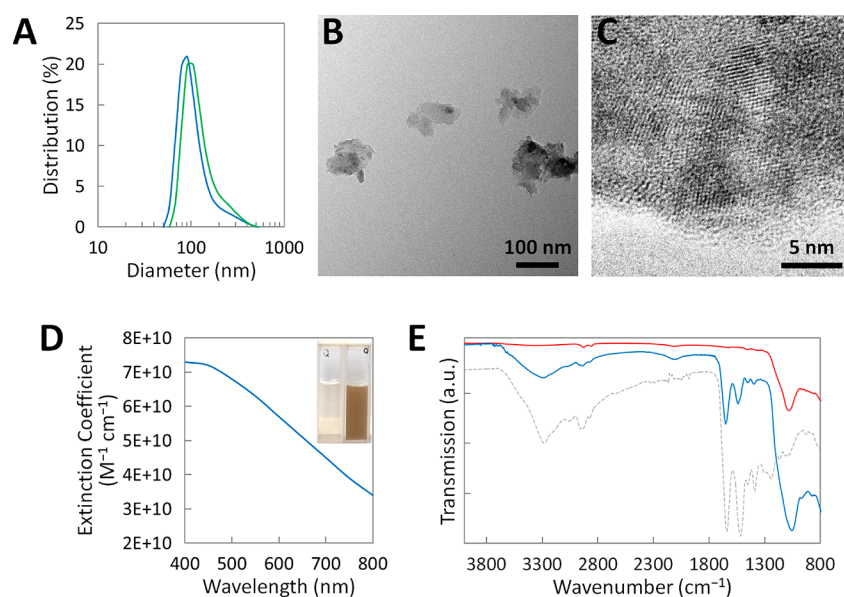
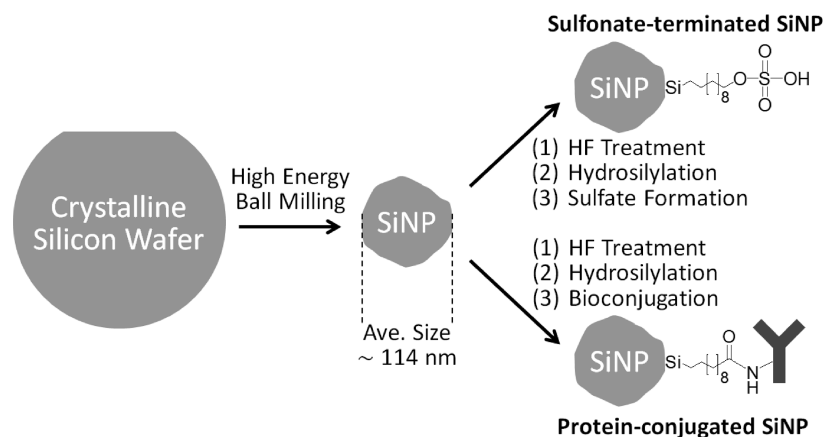


Figure 1. (A) DLS particle size distributions of the sulfonate-terminated SiNPs (blue line) and the BSA-coated SiNPs (green line) in water, respectively. (B) TEM image of an ensemble of the SiNPs. (C) High-resolution TEM image focused at the surface of one representative SiNP. (D) Extinction coefficient spectrum of the sulfonate-terminated SiNPs in water. Inset: photographs of the SiNP suspensions in water with concentrations equal to 5 and 50 $\mu\text{g mL}^{-1}$, respectively. (E) ATR-FTIR spectra of the sulfonate-terminated SiNPs (red line), the BSA-coated SiNPs (blue line), and pure BSA powder (gray dashed line), respectively.

usually exhibit stronger photoacoustic signals compared to the normal tissues.¹² However, when the biological tissues cannot efficiently absorb excitation light, employing exogenous light absorbers as contrast agents becomes necessary.

Previously, organic compounds having strong infrared absorption, such as indocyanine green (ICG), polypyrrole, and Prussian blue, have been used as contrast agents in photoacoustic imaging, by which angiography of animal brain vasculature has been demonstrated.^{13–15} On the other hand, inorganic noble-metallic nanostructures with surface plasmon resonance (SPR)-enhanced absorption, such as gold nanocages, silver nanoplates, silver bumpy nanoshells, and core–shell palladium–gold nanoplates, have also been applied as photoacoustic contrast agents for various *in vivo* imaging applications, including tomography of the cerebral cortex, visualization of tumors, and identification of lymph nodes.^{16–19} Furthermore, photoacoustic molecular imaging using carbon nanotubes has been realized.²⁰ However, so far relatively less

attention has been given to photoacoustic contrast agents based on semiconductors.²¹

In this work, we demonstrate high contrast and high-resolution OR-PAM imaging of zebrafish and cancer cells by using silicon nanoparticles (SiNPs) as contrast agents. Owing to the indirect band gap nature of silicon, the pulsed excitation light absorbed by the SiNPs is efficiently converted into heat, which in turn causes the thermoelastic expansion of biological tissues and the emission of ultrasonic waves. Compared to the organic dyes, the SiNPs as light absorbers are less vulnerable to photobleaching and have higher extinction coefficients due to silicon's large transition dipole moments and high refractive indices at the optical wavelengths.²² Furthermore, the silicon-based nanomaterials in general are more biocompatible than the noble-metal- or carbon-based ones^{23–25} and have versatile surface chemistry for functionalization.²⁶ It is worth mentioning that mesoporous SiNPs have also been used as encapsulating structures for the loading of molecular photoacoustic contrast agents.²⁷

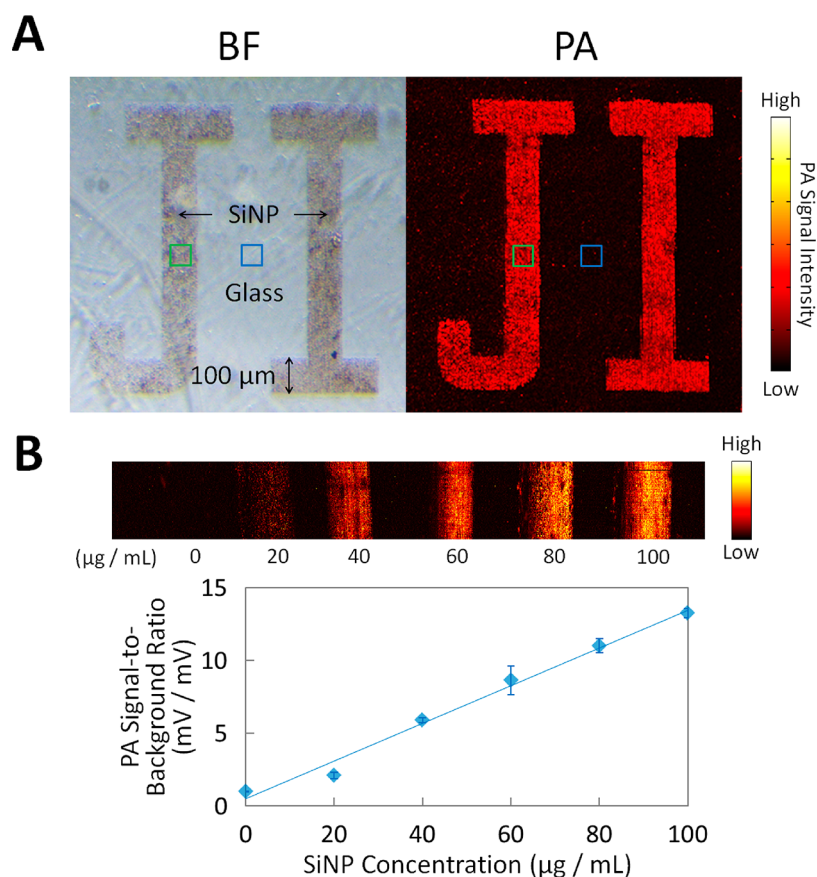


Figure 2. (A) Bright-field (BF) and photoacoustic (PA) images of the “JI” pattern fabricated by self-assembly of the SiNPs on a photolithography-patterned glass substrate. The signal-to-background ratio is defined as the average signal intensity in the green square area versus the average signal intensity in the blue square area. The “JI” stands for the “UM-SJTU Joint Institute”. Here the energy of the 532 nm focused laser pulses for optical excitation was about 30 nJ per pulse at 1 kHz. (B) Photoacoustic images and signal-to-background ratios of the SiNP suspensions in water with different concentrations. The SiNP suspensions were loaded in clear plastic tubes with inner diameters equal to 0.5 mm. The photoacoustic signals measured by the hydrophone have the unit of millivolts (mV). At 0 $\mu\text{g mL}^{-1}$, the signal-to-background ratio was close to one, showing that the photoacoustic signal resulting from the empty tube is indistinguishable as compared to the background. Here the energy of the 532 nm focused laser pulses for optical excitation was about 150 nJ per pulse at 1 kHz.

Here the SiNPs were synthesized by high-energy ball milling of crystalline silicon wafers (Scheme 1). The top-down approach can easily mass produce monodisperse SiNPs, while ensuring each nanoparticle has high crystallinity. After surface functionalization, the SiNPs became water-soluble and able to be conjugated with biomolecules for various OR-PAM imaging applications, including tracing of live zebrafish embryonic cells microinjected with the sulfonate-terminated SiNPs, photoacoustic-fluorescence dual-modality imaging of live zebrafish larvae microinjected with a mixture of the bovine serum albumin (BSA)-coated SiNPs and dextran-rhodamine dyes, and immuno-photoacoustic imaging of cancer cells immunostained with the antibody-conjugated SiNPs. These results suggest that the surface-functionalized SiNPs can be used as benign and efficient photoacoustic contrast agents for a wide variety of biomedical applications.

EXPERIMENTAL RESULTS

Synthesis and Characterizations of the SiNPs. The synthesis and functionalization of the SiNPs are illustrated in Figure S1 and described in detail in the Experimental Section of the Supporting Information. After high-energy ball milling (Figure S1A), followed by hydrosilylation with 10-undecen-1-ol (UDO) and surface treatment by chlorosulfonic acid (Figure S1B), the sulfonate-terminated SiNPs were highly hydrophilic and able to maintain uniform and stable

suspension in water. The dynamic light-scattering (DLS) particle size distribution revealed that the vast majority of the SiNPs had sizes less than 200 nm, with an average particle size of about 114 nm (blue line in Figure 1A). The transmission electron microscopy (TEM) images showed that the SiNPs were characterized with irregular shapes (Figure 1B) and polycrystalline surfaces (Figure 1C). The SiNP surface was slightly porous, with the specific surface area equal to $122.6 \text{ m}^2 \text{ g}^{-1}$, as measured by a standard Brunauer–Emmett–Teller (BET) method. The X-ray powder diffraction (XRD) analysis further confirmed that the SiNPs were polycrystalline, despite the fact that their source material, the silicon wafer, was single crystalline (Figure S2).²⁸ Such a transformation of crystallinity may be caused by the change of surface strain during the milling process, which was also observed for the milled Ti_2O_3 nanoparticles.²⁹

It is worth mentioning that in the literature prolonged high-energy ball milling has also been applied to scale down the sizes of porous silicon nanoparticles and to fabricate luminescent silicon quantum dots.^{30,31} In this work, since the SiNPs were used as light absorbers rather than emitters, the milling condition was controlled in such a way that the resulting particle sizes, as shown Figure 1A, were comparable to the excitation wavelength for enhanced light-scattering and trapping effects. Furthermore, due to the high refractive indices of silicon at the optical wavelengths, which can potentially lead to Mie resonance,³² the SiNPs in water showed high extinction coefficients, particularly about $6.5 \times 10^{10} \text{ M}^{-1} \text{ cm}^{-1}$ at 532 nm, which was the excitation wavelength used for the OR-PAM imaging in this work (Figures 1D and S3). As a comparison, plasmonic gold nanoparticles

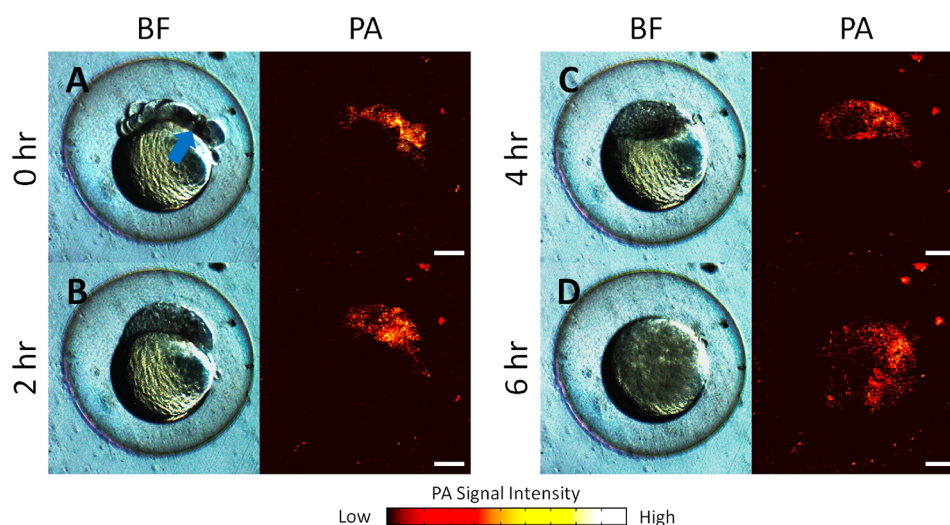


Figure 3. Time-lapse bright-field (BF) and photoacoustic (PA) images of a representative zebrafish embryo at (A) 0 h, (B) 2 h, (C) 4 h, and (D) 6 h after its embryonic cells were microinjected with the sulfonate-terminated SiNPs. The 0 h is set as the time when the imaging started. The blue arrow indicates the microinjection site. The scale bars are 200 μm . Here the energy of the 532 nm focused laser pulses for optical excitation was about 200 nJ per pulse at 1 kHz.

in water with 34 nm diameter showed an extinction coefficient of about $6.1 \times 10^9 \text{ M}^{-1} \text{ cm}^{-1}$ at 506 nm.³³

The SiNPs can be conjugated with biomolecules through a standard amide bond formation reaction (Figure S1C). The surface chemistry of the sulfonate-terminated and the BSA-coated SiNPs was characterized by using Fourier-transform infrared spectroscopy with attenuated total reflection (ATR-FTIR), respectively. The sulfonate-terminated SiNPs (red line in Figure 1E) showed a primary infrared absorption peak at 1100 cm^{-1} (Si–O–Si stretching), in combination with other minor peaks at 1350 cm^{-1} (S=O stretching), 1450 cm^{-1} (C–H deformation), 2100 cm^{-1} (Si–H stretching), 2855 and 2925 cm^{-1} (C–H stretching), and 3300 cm^{-1} (O–H stretching). These peaks represent the intrinsic surface chemistry of the SiNPs and confirm the alkyl passivation and sulfonate terminations. Particularly, the 1100 cm^{-1} absorption peak associated with the Si–O–Si bonds was also found in photoluminescent silicon quantum dots.^{31,34} On the other hand, the infrared absorption spectrum of the BSA-coated SiNPs (blue line in Figure 1E) was essentially a combination of the absorption spectra from pure BSA powder (gray dashed line in Figure 1E) and the sulfonate-terminated SiNPs. Furthermore, with the BSA coating, the average particle size of the SiNPs increased from about 114 nm of the sulfonate-terminated SiNPs to about 129 nm (green line in Figure 1A). Both results confirm that the BSA molecules were indeed conjugated to the SiNP surfaces.

Photoacoustic Imaging with the SiNPs as Contrast Agents.

Prior to imaging of biological samples, the efficacy of the SiNPs as photoacoustic contrast agents was verified by using a customized OR-PAM imaging system (Figure S4). First, the sulfonate-terminated SiNPs were deposited on a photolithography-patterned glass substrate by electrostatic layer-by-layer self-assembly. Under the bright field, the “JI” pattern formed by the self-assembled SiNPs exhibited slightly darker color as compared to the glass background, with a grayscale signal-to-background ratio of about 1.2 (Figure 2A). In contrast, under the OR-PAM, the “JI” pattern obviously stood out from the background, and the photoacoustic signal-to-background ratio drastically improved to about 7.7 (Figure 2A). Furthermore, the “JI” geometry obtained under the OR-PAM was identical to that obtained under the bright field, showcasing the high-resolution capability of the OR-PAM imaging system (Figure S5). Second, the photoacoustic images of the SiNP suspensions in water with different concentrations were obtained, and the corresponding photoacoustic signal-to-background ratios were measured (Figure 2B). For the SiNP concentration as low as $40 \mu\text{g mL}^{-1}$, a well-detectable signal-to-background ratio of more than 5 was able to be achieved.

Furthermore, the signal-to-background ratio linearly increased as the SiNP concentration increased. In comparison, under the same imaging conditions, a similar contrast can also be achieved by using gold nanospheres as the contrast agents, but with the molar concentration of the gold nanospheres much higher than that of the SiNPs (Figure S6).

Tracing of Zebrafish Embryonic Cells. Cell tracing in stem cell research is an important technique to identify the location of implanted cells and distinguish them from endogenous cells.³⁵ Apart from the current approaches, such as loading with fluorescent probes, expressing fluorescent proteins, and gene sequencing of cellular barcodes,³⁶ in this work we demonstrate a novel cell tracing method based on OR-PAM. We used the SiNPs as the high-contrast tracer and live zebrafish embryos as the model (Figure 3). First, the sulfonate-terminated SiNP suspension in water was microinjected to the zebrafish embryonic cells. The injected embryo was further incubated for 1.5 h and then fixed in low melting agarose gel and put under the OR-PAM imaging system (Figure S4) for acquiring the time-lapse photoacoustic images. As the embryo developed and the embryonic cells proliferated, the locations of the cells carrying the SiNPs can be clearly traced by the spread of the photoacoustic signals (Figure 3A to 3D). Since the photoacoustic signals matched well with the locations of the cells shown in the bright-field images and only a portion of the cellular part of the embryo carried obvious photoacoustic signals, the spread of the SiNPs should be mainly due to cell division rather than diffusion. No adverse effects due to the microinjection had been observed as compared to the normal embryos. While the cell tracing can also be accomplished by using fluorescent probes, such as dextran-rhodamine dyes (Figure S7), the contrast was hampered by autofluorescence which is usually most prominent at the yolk sac of a zebrafish embryo. Even with proper optical filters applied, the yolk sac autofluorescence was still noticeable, and only a moderate fluorescence signal-to-background ratio of about 7.5 was achieved (Figure S7A). In contrast, under the OR-PAM, no detectable signal was found at the yolk sac where there was no SiNP, yielding a much higher photoacoustic signal-to-background ratio of about 44.6 (Figure S7B).

Photoacoustic-Fluorescence Dual-Modality Imaging of Zebrafish Larvae. Photoacoustic and fluorescence are two imaging modalities different in contrast mechanism but potentially complementary to each other. Previously, heterostructured probes, such as peroxyxynitrite-sensitive CySO_3CF_3 , fluorogens with aggregation-induced emission and dye-loaded perfluorocarbon nanoparticles, have shown the synergies between the two imaging modalities on

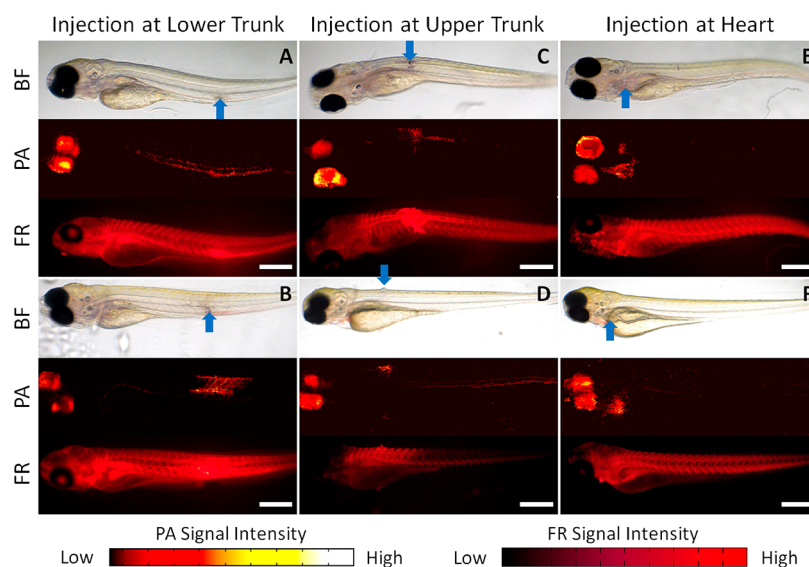


Figure 4. Bright-field (BF), photoacoustic (PA), and fluorescence (FR) images of zebrafish larvae microinjected with a mixture of the BSA-coated SiNPs and dextran-rhodamine dye at (A and B) the lower trunk, (C and D) the upper trunk, and (E and F) the heart regions, respectively. The different rows correspond to different zebrafish samples. The blue arrows indicate the microinjection sites. The scale bars are 500 μm . Here the energy of the 532 nm focused laser pulses for optical excitation was about 150 nJ per pulse at 1 kHz.

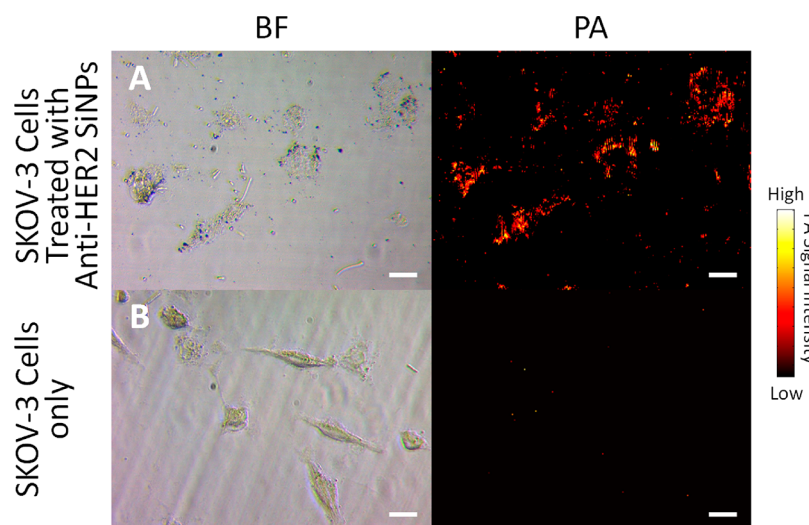


Figure 5. Bright-field (BF) and photoacoustic (PA) images of (A) the SKOV-3 cancer cells treated with the anti-HER2-conjugated SiNPs and (B) the SKOV-3 cancer cells only. The scale bars are 25 μm . Here the energy of the 532 nm focused laser pulses for optical excitation was about 100 nJ per pulse at 1 kHz.

various biological samples.^{37–39} In this work, we demonstrate photoacoustic-fluorescence dual-modality imaging of live zebrafish larvae which were microinjected at different locations with a premixed mixture of the BSA-coated SiNPs and dextran-rhodamine dyes (Figure 4). The SiNPs were coated with BSA for the better antifouling property.³¹ Experimentally, when the sulfonate-terminated SiNPs were used instead, aggregates of the SiNPs and dye molecules were formed prior to the microinjection, likely due to strong ionic interaction between the two materials. In contrast, the BSA-coated SiNPs maintained very stable suspension before and after mixing with the dextran-rhodamine dyes. The injected larvae were further incubated for 30 min, fixed in low melting agarose gel, and then put under a macrozoom fluorescence microscope (Olympus MVX10) and the OR-PAM imaging system (Figure S4) for acquiring the fluorescence and photoacoustic images, respectively. No adverse effects due to the microinjection had been observed as compared to the normal larvae. Due to the large difference in size, the two agents exhibited very different biodistributions after being injected at the

same instant. In contrast to the dye molecules which diffused in the tissues and circulated over the whole fish body quickly, the BSA-coated SiNPs were mostly contained in vessels or tissues around the injection sites within a few hours after injection. For example, when injected at the lower trunk region, the BSA-coated SiNPs were found evenly distributed in a short range of trunk lymphatic networks or intersegmental vessels (Figure 4A and 4B). On the other hand, when injected at the upper trunk region, the BSA-coated SiNPs were essentially trapped in the muscle tissues close to the injection sites (Figure 4C and 4D). In contrast, here the dextran-rhodamine dyes showed different fluorescence signal distributions, likely because in one case the injection happened primarily in the muscle tissue (FR in Figure 4D), while in the other case the injection reached near a vessel of the zebrafish circulatory system (FR in Figure 4C). Interestingly, when injected at the heart region, the BSA-coated SiNPs did not circulate along with the dye molecules, likely because they were immediately retained by the nearby liver, which as a mononuclear phagocytic system (MPS) organ filters circulating nanoparticles

(Figure 4E and 4F).⁴⁰ In addition to the particle size, another possible cause for the relatively contained biodistributions observed for the SiNPs might be their BSA coatings, which as foreign proteins may induce immune response in the injected zebrafish which can further enlarge the particle size and impede the movement of the SiNPs. Having two drastically different biodistributions displayed by two complementary imaging modalities can be helpful to pharmacokinetic studies on how the particle size affects the absorption, distribution, and excretion of the agents.

Immuno-Photoacoustic Imaging of Cancer Cells. The diagnostic accuracy of the immunofluorescence technique is greatly affected by autofluorescence. Previously, several approaches have been proven effective to alleviate the issue, such as using fluorophores emitting in the near-infrared wavelengths where the autofluorescence is relatively weak and removing the short-lived autofluorescence by time gating.^{41,42} By taking advantage of OR-PAM's high contrast attribute, in this work we demonstrate immuno-photoacoustic imaging which is exempt from autofluorescence (Figure 5). First, SKOV-3 cancer cells which overexpress HER2 antigens were immunostained with the anti-HER2-conjugated SiNPs. After being fixed with paraformaldehyde and washed by phosphate-buffered saline with Tween-20 (PBST), the cells were put under the OR-PAM imaging system (Figure S4) for acquiring the photoacoustic images. The SKOV-3 cancer cells treated with the anti-HER2 conjugated SiNPs showed obvious photoacoustic signals on the cell membranes (Figure 5A), whereas no photoacoustic signals were found for the cells only (Figure 5B). In comparison, CHO cells without HER2 antigens were also treated by the anti-HER2 conjugated SiNPs following the same procedure, but only weak and randomly distributed photoacoustic signals due to the nonspecific binding were observed (Figure S8). Furthermore, no photoacoustic signal was detected for either SKOV-3 or CHO cells treated by the BSA-coated SiNPs, showing that it was the conjugation with anti-HER2 that resulted in the accumulation of the SiNPs on the SKOV-3 cells (Figure S9). The above results show that the immuno-photoacoustic imaging can be an autofluorescence-free alternative to the conventional immunofluorescence imaging.

Comparison between the SiNPs and Other Photoacoustic Contrast Agents. Compared to other types of photoacoustic contrast agents which might also be able to demonstrate similar functionalities as shown here, the SiNPs possess three main advantages, including high photothermal stability, wide photoacoustic excitation range, and low cytotoxicity. After repeated (36 times) photoacoustic imaging of the same SiNP suspension by using the 532 nm focused laser pulses with relatively high power (100 or 200 nJ per pulse, 1 kHz), about 40% of the photoacoustic signal intensity was able to be conserved (Figure S10). When the power of the laser pulses was relatively low (20 nJ per pulse, 1 kHz), the signal intensity can be very stable throughout numerous raster scanning cycles (Figure S11). In comparison, the infrared absorbing dyes (e.g., ICG) and the noble-metallic nanostructures (e.g., gold nanorods), when used as photoacoustic contrast agents, may have less photothermal stability because of photobleaching and change of surface plasmon resonant structures.^{43,44} Furthermore, the SiNPs maintain high extinction coefficients (more than $2 \times 10^{10} \text{ M}^{-1} \text{ cm}^{-1}$) from the visible to near-infrared spectral range (Figure 1D), and the photoacoustic signal intensity is nearly proportional to the extinction coefficient (Figure S12), suggesting that the SiNPs can be efficient photoacoustic contrast agents with not only visible but also near-infrared photoexcitation. To confirm this, we demonstrate AR-PAM imaging of a thin SiNP-loaded tube buried underneath a chicken breast layer with the thickness of about 2–3 mm by using 670 and 770 nm laser pulses, respectively (Figure S13). The AR-PAM imaging system is illustrated in Figure S14. Compared to the OR-PAM, the AR-PAM imaging achieves higher penetration depth but lower spatial resolution. With the chicken breast thickness of about 2 mm, which is larger than the optical transport mean free path (about 1 mm), clear images of the SiNPs can be obtained by using either excitation wavelength. However, as the thickness gradually increased to about 3 mm, the photoacoustic signal intensity decreased accordingly. Lastly,

the cytotoxicity of the SiNPs was evaluated by a cell viability assay (Figure S15). The BSA-coated SiNPs exhibited an inhibitory particle concentration, corresponding to 50% cell viability (IC_{50}), about $105 \mu\text{g mL}^{-1}$, which is comparable to the IC_{50} of other silicon nanomaterials and higher than the IC_{50} of other heavy metal containing quantum dots (about 10 to 20 $\mu\text{g/mL}$).⁴⁵

CONCLUSION

In summary, we demonstrate high contrast and high-resolution OR-PAM imaging by using the SiNPs as contrast agents. The SiNPs were synthesized by high-energy ball milling of crystalline silicon wafers, followed by hydrosilylation with bifunctional olefinic ligands to enable water solubility and bioconjugation. The SiNPs with irregular shapes had an average particle size of about 114 nm. The SiNP surfaces were polycrystalline and slightly porous, with the specific surface area equal to $122.6 \text{ m}^2 \text{ g}^{-1}$. Furthermore, the SiNPs in water showed remarkably high extinction coefficients, particularly about $6.5 \times 10^{10} \text{ M}^{-1} \text{ cm}^{-1}$ at 532 nm, which was the excitation wavelength used for the OR-PAM imaging in this work. The intrinsic surface chemistry of the SiNPs was predominantly associated with the Si–O–Si bonds (1100 cm^{-1}), and the conjugation to biomolecules, such as BSA and antibodies, was accomplished through the amide bond formation reaction. Different OR-PAM imaging applications based on the surface-functionalized SiNPs were demonstrated, including (1) tracing of live zebrafish embryonic cells microinjected with the sulfonate-terminated SiNPs, (2) photoacoustic-fluorescence dual-modality imaging of live zebrafish larvae microinjected with a mixture of the BSA-coated SiNPs and dextran-rhodamine dyes, and (3) immuno-photoacoustic imaging, as an autofluorescence-free alternative to the conventional immunofluorescence imaging, of cancer cells immunostained with the antibody-conjugated SiNPs. Lastly, the photothermal stability, photoacoustic excitation range, and cytotoxicity of the SiNPs were characterized, and additional AR-PAM imaging of the SiNPs buried underneath a chicken breast layer with the thickness larger than the optical transport mean free path (about 1 mm) was demonstrated. These results suggest that the surface-functionalized SiNPs can be used as benign and efficient photoacoustic contrast agents for a wide variety of biomedical applications.

ASSOCIATED CONTENT

Supporting Information

The Supporting Information is available free of charge at <https://pubs.acs.org/doi/10.1021/acsanm.9b01682>.

Synthesis and functionalization of the SiNPs. XRD patterns of the crystalline silicon wafer and the SiNPs. Absorbance spectra of the SiNP suspensions in water with different concentrations. Schematic and resolution measurement of the OR-PAM imaging system. Comparison between the fluorescence and photoacoustic images of the microinjected zebrafish embryos. Bright-field and photoacoustic images of the CHO cells with and without the treatment of the anti-HER2 conjugated SiNPs. Bright-field and photoacoustic images of the SKOV-3 and the CHO cells treated with the BSA-coated SiNPs. Photothermal stability and photoacoustic excitation range of the SiNPs. AR-PAM imaging of the SiNPs buried under a chicken breast layer. Cell viability assay for the SiNPs (PDF)

AUTHOR INFORMATION

Corresponding Authors

*Email: changching.tu@sjtu.edu.cn. Tel: +86-21-34206765 Ext. 5081.

*Email: sungliang.chen@sjtu.edu.cn. Tel: +86-21-34206765 Ext. 4281.

ORCID

Sung-Liang Chen: 0000-0002-0572-5110

Chang-Ching Tu: 0000-0002-9233-1928

Notes

The authors declare no competing financial interest.

ACKNOWLEDGMENTS

This research was financially supported by the Shanghai Pujiang Talent Program (18PJ1404900) and the National Natural Science Foundation of China (NSFC) (61775134). The authors thank C.-C. Tu and Y. Xu for proposing the original idea, synthesis and characterization of the SiNPs, and preparation and submission of the final manuscript; S.-L. Chen and Z. Ye for implementation and optimization of the OR-PAM imaging system, image acquisition, and composition of the first manuscript draft; and L. Jing, P. K. Srivastava, and W. Wang for preparing the biological samples.

REFERENCES

- (1) Xu, M. H.; Wang, L. V. Photoacoustic Imaging in Biomedicine. *Rev. Sci. Instrum.* **2006**, *77*, No. 041101.
- (2) Wang, L. V. *Photoacoustic Imaging and Spectroscopy*; CRC Press, 2009.
- (3) Wang, L. V.; Hu, S. Photoacoustic Tomography: in Vivo Imaging from Organelles to Organs. *Science* **2012**, *335*, 1458–1462.
- (4) Yao, J. J.; Wang, L. V. Photoacoustic Microscopy. *Laser Photonics Rev.* **2013**, *7*, 758–778.
- (5) Park, S.; Lee, C.; Kim, J.; Kim, C. Acoustic Resolution Photoacoustic Microscopy. *Biomed. Eng. Lett.* **2014**, *4*, 213–222.
- (6) Hu, S.; Maslov, K.; Wang, L. V. Second-Generation Optical-Resolution Photoacoustic Microscopy with Improved Sensitivity and Speed. *Opt. Lett.* **2011**, *36*, 1134–1136.
- (7) Wang, L. V. Multiscale Photoacoustic Microscopy and Computed Tomography. *Nat. Photonics* **2009**, *3*, 503–509.
- (8) Zhang, H. F.; Maslov, K.; Stoica, G.; Wang, L. V. Functional Photoacoustic Microscopy for High-Resolution and Noninvasive in Vivo Imaging. *Nat. Biotechnol.* **2006**, *24*, 848–851.
- (9) Wong, T. T. W.; Zhang, R.; Hai, P.; Zhang, C.; Pleitez, M. A.; Aft, R. L.; Novack, D. V.; Wang, L. V. Fast Label-Free Multilayered Histology-Like Imaging of Human Breast Cancer by Photoacoustic Microscopy. *Sci. Adv.* **2017**, *3*, No. e1602168.
- (10) Kim, C.; Cho, E. C.; Chen, J. Y.; Song, K. H.; Au, L.; Favazza, C.; Zhang, Q.; Copley, C. M.; Gao, F.; Xia, Y. N.; Wang, L. V. In Vivo Molecular Photoacoustic Tomography of Melanomas Targeted by Bioconjugated Gold Nanocages. *ACS Nano* **2010**, *4*, 4559–4564.
- (11) Yao, J.; Wang, L.; Yang, J.-M.; Maslov, K. I.; Wong, T. T. W.; Li, L.; Huang, C.-H.; Zhou, J.; Wang, L. V. High-Speed Label-Free Functional Photoacoustic Microscopy of Mouse Brain in Action. *Nat. Methods* **2015**, *12*, 407–410.
- (12) Wang, X.; Pang, Y.; Ku, G.; Xie, X.; Stoica, G.; Wang, L. V. Noninvasive Laser-Induced Photoacoustic Tomography for Structural and Functional in Vivo Imaging of the Brain. *Nat. Biotechnol.* **2003**, *21*, 803–806.
- (13) Wang, X.; Ku, G.; Wegiel, M. A.; Bornhop, D. J.; Stoica, G.; Wang, L. V. Noninvasive Photoacoustic Angiography of Animal Brains in Vivo with Near-Infrared Light and an Optical Contrast Agent. *Opt. Lett.* **2004**, *29*, 730–732.
- (14) Zha, Z.; Deng, Z.; Li, Y.; Li, C.; Wang, J.; Wang, S.; Qu, E.; Dai, Z. Biocompatible Polypyrrole Nanoparticles as a Novel Organic Photoacoustic Contrast Agent for Deep Tissue Imaging. *Nanoscale* **2013**, *5*, 4462–4467.
- (15) Liang, X.; Deng, Z.; Jing, L.; Li, X.; Dai, Z.; Li, C.; Huang, M. Prussian Blue Nanoparticles Operate as a Contrast Agent for Enhanced Photoacoustic Imaging. *Chem. Commun.* **2013**, *49*, 11029–11031.
- (16) Yang, X.; Skrabalak, S. E.; Li, Z.-Y.; Xia, Y.; Wang, L. V. Photoacoustic Tomography of a Rat Cerebral Cortex in Vivo with Au Nanocages as an Optical Contrast Agent. *Nano Lett.* **2007**, *7*, 3798–3802.
- (17) Homan, K. A.; Souza, M.; Truby, R.; Luke, G. P.; Green, C.; Vreeland, E.; Emelianov, S. Silver Nanoplate Contrast Agents for in Vivo Molecular Photoacoustic Imaging. *ACS Nano* **2012**, *6*, 641–650.
- (18) Cha, M. G.; Lee, S.; Park, S.; Kang, H.; Lee, S. G.; Jeong, C.; Lee, Y.-S.; Kim, C.; Jeong, D. H. A Dual Modal Silver Bumpy Nanoprobe for Photoacoustic Imaging and SERS Multiplexed Identification of in Vivo Lymph Nodes. *Nanoscale* **2017**, *9*, 12556–12564.
- (19) Chen, M.; Tang, S.; Guo, Z.; Wang, X.; Mo, S.; Huang, X.; Liu, G.; Zheng, N. Core-Shell Pd@Au Nanoplates as Theranostic Agents for In-Vivo Photoacoustic Imaging, CT Imaging, and Photothermal Therapy. *Adv. Mater.* **2014**, *26*, 8210–8216.
- (20) De La Zerna, A.; Zavaleta, C.; Keren, S.; Vaithilingam, S.; Bodapati, S.; Liu, Z.; Levi, J.; Smith, B. R.; Ma, T.-J.; Oralkan, O.; Cheng, Z.; Chen, X.; Dai, H.; Khuri-Yakub, B. T.; Gambhir, S. S. Carbon Nanotubes as Photoacoustic Molecular Imaging Agents in Living Mice. *Nat. Nanotechnol.* **2008**, *3*, 557–562.
- (21) Ku, G.; Zhou, M.; Song, S.; Huang, Q.; Hazle, J.; Li, C. Copper Sulfide Nanoparticles As a New Class of Photoacoustic Contrast Agent for Deep Tissue Imaging at 1064 nm. *ACS Nano* **2012**, *6*, 7489–7496.
- (22) Resch-Genger, U.; Grabolle, M.; Cavaliere-Jaricot, S.; Nitschke, R.; Nann, T. Quantum Dots versus Organic Dyes as Fluorescent Labels. *Nat. Methods* **2008**, *5*, 763–775.
- (23) Liu, J.; Erogbogbo, F.; Yong, K.-T.; Ye, L.; Liu, J.; Hu, R.; Chen, H.; Hu, Y.; Yang, Y.; Yang, J.; Roy, I.; Karker, N. A.; Swihart, M. T.; Prasad, P. N. Assessing Clinical Prospects of Silicon Quantum Dots: Studies in Mice and Monkeys. *ACS Nano* **2013**, *7*, 7303–7310.
- (24) Fratoddi, I.; Venditti, I.; Cametti, C.; Russo, M. V. How Toxic Are Gold Nanoparticles? The State of the Art. *Nano Res.* **2015**, *8*, 1771–1799.
- (25) Kobayashi, N.; Izumi, H.; Morimoto, Y. Review of Toxicity Studies of Carbon Nanotubes. *J. Occup. Health* **2017**, *59*, 394–407.
- (26) Buriak, J. M. Organometallic Chemistry on Silicon and Germanium Surfaces. *Chem. Rev.* **2002**, *102*, 1272–1308.
- (27) Kang, J.; Kim, D.; Wang, J.; Han, Y.; Zuidema, J. M.; Hariri, A.; Park, J.-H.; Jokerst, J. V.; Sailor, M. J. Enhanced Performance of a Molecular Photoacoustic Imaging Agent by Encapsulation in Mesoporous Silicon Nanoparticles. *Adv. Mater.* **2018**, *30*, 1800512.
- (28) Westra, J. M.; Vavrunková, V.; Šutta, P.; van Swaaij, R. A. C. M. M.; Zeman, M. Formation of Thin-Film Crystalline Silicon on Glass Observed by in Situ XRD. *Energy Procedia* **2010**, *2*, 235–241.
- (29) Wang, J.; Li, Y.; Deng, L.; Wei, N.; Wang, Y.; Dong, S.; Qi, D.; Qiu, J.; Chen, X.; Wu, T. High-Performance Photothermal Conversion of Narrow-Bandgap Ti₂O₃ Nanoparticles. *Adv. Mater.* **2017**, *29*, 1603730.
- (30) Heintz, A. S.; Fink, M. J.; Mitchell, B. S. Mechanochemical Synthesis of Blue Luminescent Alkyl/Alkenyl-Passivated Silicon Nanoparticles. *Adv. Mater.* **2007**, *19*, 3984–3988.
- (31) Tu, C.-C.; Chen, K.-P.; Yang, T.-A.; Chou, M.-Y.; Lin, L. Y.; Li, Y.-K. Silicon Quantum Dot Nanoparticles with Antifouling Coatings for Immunostaining on Live Cancer Cells. *ACS Appl. Mater. Interfaces* **2016**, *8*, 13714–13723.
- (32) Baranov, D. G.; Zuev, D. A.; Lepeshov, S. I.; Kotov, O. V.; Krasnok, A. E.; Evlyukhin, A. B.; Chichkov, B. N. All-Dielectric Nanophotonics: the Quest for Better Materials and Fabrication Techniques. *Optica* **2017**, *4*, 814–825.

(33) Liu, X.; Atwater, M.; Wang, J.; Huo, Q. Extinction Coefficient of Gold Nanoparticles with Different Sizes and Different Capping Ligands. *Colloids Surf., B* **2007**, *58*, 3–7.

(34) Kusová, K.; Cibulka, O.; Dohnalová, K.; Pelant, I.; Valenta, J.; Fučíková, A.; Zidek, K.; Lang, J.; Englich, J.; Matejka, P.; Štěpánek, P.; Bakardjieva, S. Brightly Luminescent Organically Capped Silicon Nanocrystals Fabricated at Room Temperature and Atmospheric Pressure. *ACS Nano* **2010**, *4*, 4495–4504.

(35) Yan, L.; Han, Y.; He, Y.; Xie, H.; Liu, J.; Zhao, L.; Wang, J.; Gao, L.; Fan, D. Cell Tracing Techniques in Stem Cell Transplantation. *Stem Cell Rev.* **2007**, *3*, 265–269.

(36) Marx, V. Stem Cells: Lineage Tracing Lets Single Cells Talk about Their Past. *Nat. Methods* **2018**, *15*, 411–414.

(37) Zhang, J.; Zhen, X.; Zeng, J.; Pu, K. A Dual-Modal Molecular Probe for Near-Infrared Fluorescence and Photoacoustic Imaging of Peroxynitrite. *Anal. Chem.* **2018**, *90*, 9301–9307.

(38) Li, K.; Liu, B. Polymer-Encapsulated Organic Nanoparticles for Fluorescence and Photoacoustic Imaging. *Chem. Soc. Rev.* **2014**, *43*, 6570–6597.

(39) Akers, W. J.; Kim, C.; Berezin, M.; Guo, K.; Fuhrhop, R.; Lanza, G. M.; Fischer, G. M.; Daltrozzo, E.; Zumbusch, A.; Cai, X.; Wang, L. V.; Achilefu, S. Noninvasive Photoacoustic and Fluorescence Sentinel Lymph Node Identification using Dye-Loaded Perfluorocarbon Nanoparticles. *ACS Nano* **2011**, *5*, 173–182.

(40) Park, J.-H.; Gu, L.; Maltzahn, G. V.; Ruoslahti, E.; Bhatia, S. N.; Sailor, M. J. Biodegradable Luminescent Porous Silicon Nanoparticles for in Vivo Applications. *Nat. Mater.* **2009**, *8*, 331–336.

(41) Yang, W.; Srivastava, P. K.; Han, S.; Jing, L.; Tu, C.-C.; Chen, S.-L. Optomechanical Time-Gated Fluorescence Imaging Using Long-Lived Silicon Quantum Dot Nanoparticles. *Anal. Chem.* **2019**, *91*, 5499–5503.

(42) Diao, S.; Hong, G.; Antaris, A. L.; Blackburn, J. L.; Cheng, K.; Cheng, Z.; Dai, H. Biological Imaging without Autofluorescence in the Second Near-Infrared Region. *Nano Res.* **2015**, *8*, 3027–3034.

(43) Weber, J.; Beard, P. C.; Bohndiek, S. E. Contrast Agents for Molecular Photoacoustic Imaging. *Nat. Methods* **2016**, *13*, 639–650.

(44) Moon, H.; Kumar, D.; Kim, H.; Sim, C.; Chang, J.-H.; Kim, J.-M.; Kim, H.; Lim, D.-K. Amplified Photoacoustic Performance and Enhanced Photothermal Stability of Reduced Graphene Oxide Coated Gold Nanorods for Sensitive Photoacoustic Imaging. *ACS Nano* **2015**, *9*, 2711–2719.

(45) Erogbogbo, F.; Yong, K.-T.; Roy, I.; Hu, R.; Law, W.-C.; Zhao, W.; Ding, H.; Wu, F.; Kumar, R.; Swihart, M. T.; Prasad, P. N. In Vivo Targeted Cancer Imaging, Sentinel Lymph Node Mapping and Multi-Channel Imaging with Biocompatible Silicon Nanocrystals. *ACS Nano* **2011**, *5*, 413–423.